The Variable Stiffness Actuator vsaUT-II: Mechanical Design, Modeling, and Identification

Stefan S. Groothuis, Giacomo Rusticelli, Andrea Zucchelli, Stefano Stramigioli, *Senior Member, IEEE*, and Raffaella Carloni, *Member, IEEE*

Abstract—In this paper, the rotational variable stiffness actuator vsaUT-II is presented. This actuation system is characterized by the property that the apparent stiffness at the actuator output can be varied independently from its position. This behavior is realized by implementing a variable transmission ratio between the internal elastic elements and the actuator output, i.e., a lever arm with variable pivot point position. The pivot point is moved by a planetary gears mechanism, which acquires a straight motion from only rotations, thereby providing a low-friction transmission. The working principle details of the vsaUT-II are elaborated and the design is presented. The actuator dynamics are described by means of a lumped parameter model. The relevant parameters of the actuator are estimated and identified in the physical setup and measurements are used to validate both the design and the derived model.

Index Terms—Identification, mechanical design, modeling, variable stiffness actuators.

I. INTRODUCTION

COMPLIANT actuators can be classified into two main categories: active and passive. In active compliant actuators, the compliance is achieved by control at a limited bandwidth and by relying on proper sensors. These sensors may fail and consequently may cause instability and safety issues during tasks in which the actuated load interacts with the surrounding environment or with humans. Passive compliant actuators, on the other hand, rely on mechanical elastic elements, placed between the internal motors and the actuated load. The internal mechanical compliance not only decouples the inertia of the motors from the load, thereby ensuring safety during any kind of human–robot interaction, but can also be used to store energy, especially during tasks in which the kinetic energy can be absorbed during impacts and released when needed.

Variable stiffness actuators are characterized by the ability that the apparent stiffness at the actuated load can be varied independently from its position. The internal kinematic structure of a variable stiffness actuator consists, in general, of internal motors and internal elastic elements, which determine the position and the stiffness of the load and, therefore, how the internal elastic elements are perceived at the output. The output stiffness can thus be tuned to the requirements imposed by a specific task or by the environment, while the actuated load can follow a certain trajectory.

Considerable research effort has been put into the development of variable stiffness actuators. Therefore, many different designs, based on various passive compliance principles, have been presented. Some designs rely on changing the pretension of the, in general nonlinear, internal elastic elements, e.g., MAC-CEPA [1], VSA-II [2] and VS-Joint [3]. A characteristic of these systems is that the energy is put into or extracted from the elastic elements during stiffness changes. In other designs, the number of active spring coils or the effective length of leaf springs is varied, e.g., WAM-10 [4], VSJ [5], and "Jack Spring" [6]. A characteristic of these systems is that an infinite stiffness configuration can be reached, but a zero-stiffness configuration cannot. The HDAU [7], AwAS [8], AwAS-II [9], CompAct-VSA [10], the vsaUT [11], the mVSA-UT [12], and [13] use a lever arm of variable effective length.

As described in [14] and [15], when a variable transmission ratio is realized between the actuated load and the force due to the internal elastic elements, the actuator has the property that the output stiffness can be adjusted without energy injection into or extraction from the internal elastic elements. This means that all the energy supplied by the internal motors can be used to do work on the load, without being captured and, therefore, lost in the elastic elements. To realize the variable transmission ratio, a lever arm with variable effective length can be implemented. The elements acting on the lever arm are the elastic elements, the pivot point, and the connection to the actuator output, on which the load applies the external force. By changing the individual positions along the lever arm, it is possible to change the transmission ratio between the elastic elements' force and the actuator output force and, therefore, to change the apparent output stiffness. Previous research showed that moving the pivot point along the lever arm minimizes the involved forces during a stiffness change [16].

In this paper, the variable stiffness actuator vsaUT-II based on a variable transmission ratio lever arm is presented, modeled, and identified. The main novelty of the actuator is the kinematic structure to move the pivot point along the lever arm, which is a modified planetary gears mechanism. This is presented in Section II, together with the general working principle and the
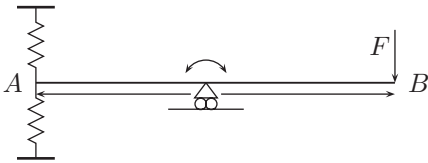
Fig. 1. Conceptual scheme of the variable transmission ratio lever arm obtained by means of the moving pivot point. The stiffness K is zero when the pivot point is at A and it is infinite when the pivot point is at B.

lever arm design. Section III presents the prototyping and design choices of the actuator. The lumped parameter model of the system is derived and identification of the system parameters is done. Further measurements on the realized prototype are presented in Section IV to show the performance and potential of the overall system. The actuator is discussed in Section V and concluding remarks are given in Section VI.

II. VSAUT-II VARIABLE STIFFNESS ACTUATOR

In this section, we present the variable stiffness actuator vsaUT-II by elaborating on its working principle and showing the various functional layers separately.

A. Working Principle

Following the discussion in [11] and [15], the design of the vsaUT-II is based on a variable transmission ratio realized between the actuated load and the force due to the internal elastic elements. By moving the pivot point position along the lever arm, it is possible to change the transmission ratio and; therefore, the apparent output stiffness felt at the load.

Fig. 1 shows a conceptual scheme of the lever arm with a variable transmission ratio, obtained by means of the moving pivot. More specifically, the figure shows a lever arm to which two elastic elements are attached at A, the output force F of the load acts at B and a pivot point that can move along the entire lever arm. The output stiffness K, felt at the output and associated to a force F and an output deflection r, is

$$K := \frac{\partial F}{\partial r}.$$

This output stiffness can be changed in a continuous way by positioning the pivot point along the lever arm. Note that: 1) the stiffness K is zero when the pivot is located at A, since the lever arm is free to rotate about its pivot point, without influencing the elongation of the springs and 2) the stiffness K is infinite when the pivot is located at B, since there is a direct transmission of forces from the output on the pivot point.

Moving the pivot point along the lever arm to obtain a variable transmission ratio minimizes the involved forces [16] and is also used in the AwAS-II and CompAct-VSA. The HDAU and vsaUT realize a variable transmission ratio by moving the application point of the output force along the lever arm, while in the AwAS the elastic elements are moved.

B. Functional System Overview

For a clear overview of the actuator, Fig. 2 shows an exploded CAD view of the vsaUT-II prototype in which the two funda-
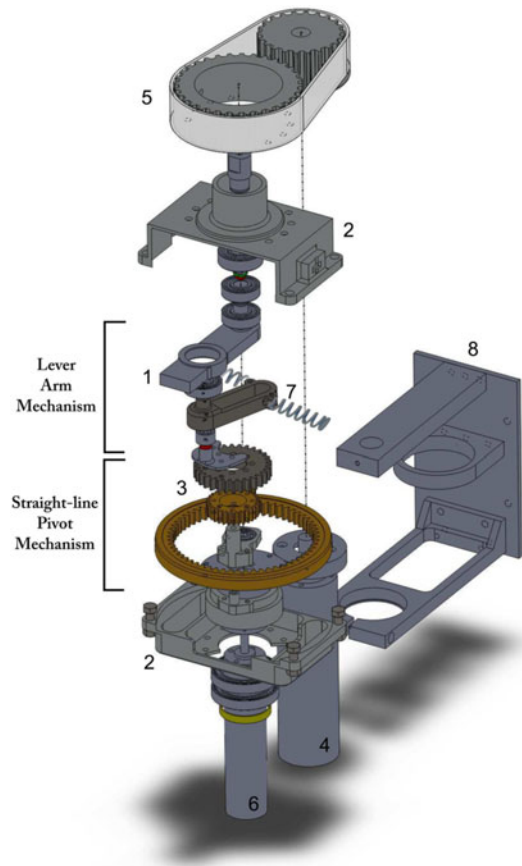

Fig. 2. Exploded view of the vsaUT-II. The labels indicate the following: 1—the actuator output; 2—the rotating actuator frame; 3—the gears mechanism; 4—motor for changing equilibrium output position; 5—timing belt transmission; 6—motor for varying output stiffness; 7—the lever arm and springs; and 8—the fixed reference frame housing.

mental actuator mechanisms are explicitly shown: the straight-line pivot mechanism and the lever arm mechanism. These layers consist of the lever arm and springs (see Fig. 1) indicated by 7, the actuator output by 1, a planetary gears mechanism by 3, and a motor to move the pivot by 6. These are elaborated in detail in the following subsections. Furthermore, 2 indicates the rotating actuator frame with respect to the fixed reference frame 8. The rotating frame is driven by motor 4 via a timing belt 5.

C. Straight-line Pivot Mechanism

As it follows from the description of the working principle, the pivot point has to move along the lever arm and, therefore, it should follow a straight-line trajectory. The vsaUT-II prototype innovates in the way this straight-line motion is achieved, with a stiff, efficient and low-friction transmission.

The pivot is moved by a planetary gears system, as shown in Fig. 3. It consists of a ring gear (the annulus) with pitch diameter D_r and a planet gear with pitch diameter $D_p = D_r/2$ to which the pivot point is connected at a distance of $D_r/4$ from the center of the planet gear. Due to this precise ratio between the pitch diameters, the pivot point moves in a straight line with respect to the ring gear when the planet gear runs along the ring gear [17]. A
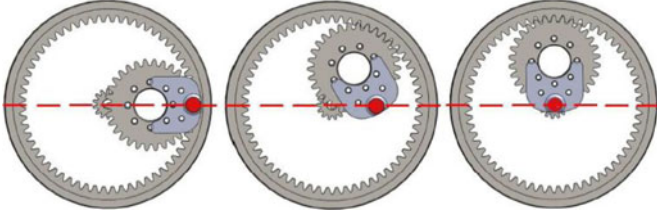
Fig. 3. Mechanism to move the pivot along the lever arm. Since the ring gear has a pitch diameter D_r twice as large as the pitch diameter of the planet gear $D_r/2$, a point on the planet gear tracks a straight line.
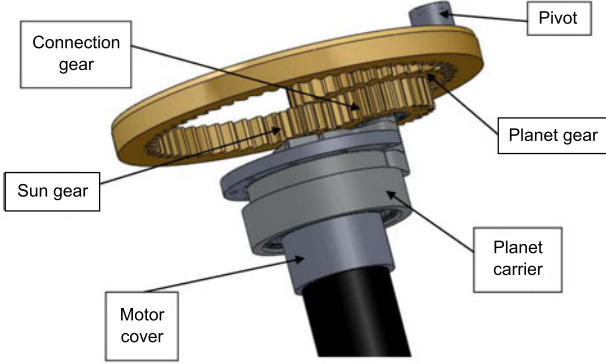

Fig. 4. View of the planetary gears system used to move the pivot point.

Fig. 5. Kinematic diagram of the planetary gears system as shown in Fig. 3. The pivot is the shaded circle associated to coordinate q_1, θ_s is the angle of the sun gear, θ_{pc} is the angle of the planet carrier, and θ_p is the angle of the planet gear.

similar (hypocycloid) mechanism is used in the HypoSEA [18], while AwAS-II uses a ball-screw and CompAct-VSA uses a rack and pinion mechanism. In a conventional planetary gear system the sun gear is in the center of the ring gear, on the same plane as the planet and ring gears. However, the necessary ratio between the pitch diameters of the gears to obtain a straight line motion prevents this and requires that the planet gear is moved by an additional connection gear, fixed under the planet gear. This way, the sun gear can be placed in the center of the ring gear in the same plane as the connection gear. As a consequence, the distance between the sun and connection gear axes is also $D_r/2$. This is done by a planet carrier that carries the connection gear and the planet gear and is free to rotate about the axis which coincides with the sun gear's rotation axis. The planet carrier rotates on a motor cover, which connects the motor to the rotating frame and also functions as a housing for the ball bearing of the planet carrier. The planet carrier keeps the planet gear and connection gear at a fixed distance from the center. Fig. 4 shows the planetary gears system used to move the pivot point. The kinematic diagram of the planetary gears system is shown in Fig. 5. The pivot is the shaded circle indicated by coordinate $q_1(t)$, $\theta_{pc}(t)$ is the angle between the center of the planet gear and straight pivot path (the dashed line), $\theta_p(t)$ is the angle between the line parallel to the straight pivot path and the pivot point, and $\theta_s(t)$ is the angle of the sun gear. The time dependence of these variables is omitted in the remainder.

The output velocity, i.e., the translational velocity of the pivot point $\dot{q}_1$, can be described in terms of the input velocity, i.e., the rotational velocity of the sun gear $\dot{\theta}_s$. In the case of a conventional planetary gears system, if the ring gear is held stationary, then the transmission ratio from the sun gear velocity $\dot{\theta}_s$ to the
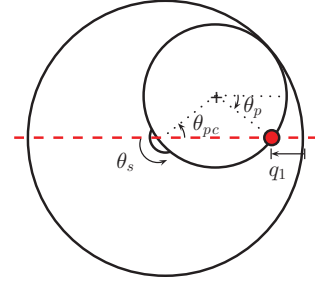
planet carrier velocity $\dot{\theta}_{pc}$, and thus also the transmission ratio from the respective angles θ_s to θ_{pc}, is given by

$$\frac{\dot{\theta}_{pc}}{\dot{\theta}_s} = \frac{\theta_{pc}}{\theta_s} = \frac{1}{1 + \frac{N_r}{N_s}}$$

where N_r and N_s are the number of ring gear and sun gear teeth, respectively [19]. However, since the planet gear is driven by a connection gear, the ratio changes to

$$\frac{\dot{\theta}_{pc}}{\dot{\theta}_s} = \frac{\theta_{pc}}{\theta_s} = \frac{1}{1 + \frac{N_r}{N_p}\frac{N_c}{N_s}} = \gamma \qquad (1)$$

where N_p and N_c are the number of planet gear and connection gear teeth, respectively. Since the output velocity $\dot{q}_1$ is the sum of the contribution of translation velocity and rotation velocity of the planet gear, it is related to $\dot{\theta}_{pc}$ and $\dot{\theta}_p$ as

$$\dot{q}_1 = \frac{1}{2}D_p \sin(\theta_{pc})\dot{\theta}_{pc} + \frac{1}{2}D_p \sin(\theta_p)\dot{\theta}_p. \qquad (2)$$

Since $D_p = D_r/2$, it holds that $\theta_p = \theta_{pc}$ and, therefore, $\dot{\theta}_p = \dot{\theta}_{pc}$. It follows that (2) becomes

$$\dot{q}_1 = D_p \sin(\theta_{pc})\dot{\theta}_{pc}. \qquad (3)$$

By using (3) and (1), this part of the system is described by

$$\dot{q}_1 = D_p \sin(\theta_{pc})\gamma\dot{\theta}_s. \qquad (4)$$

The degree of freedom q_1 is then given by

$$q_1 = -D_p \cos(\theta_{pc}) + D_p = -D_p \cos(\gamma\theta_s) + D_p. \qquad (5)$$

Equations (4) and (5) describe the output velocity $\dot{q}_1$ and position q_1, respectively, as a function of the input velocity $\dot{\theta}_s$ and the angle θ_s.

The usage of this mechanism ensures that a perfect translation motion is obtained from only a rotation, which means that only rotation actuators are needed. Furthermore, the mechanism is scalable, as shown by the mVSA-UT prototype [12].

D. Lever Arm Mechanism

Fig. 6 shows a top view of the internals of the rotating actuator frame with the connection between the lever arm, the springs, and the pivot. The pivot, with degree of freedom q_1, moves in a straight line of length l along the lever arm. One end of the lever arm is connected to the output (the blue schematic overlay) that
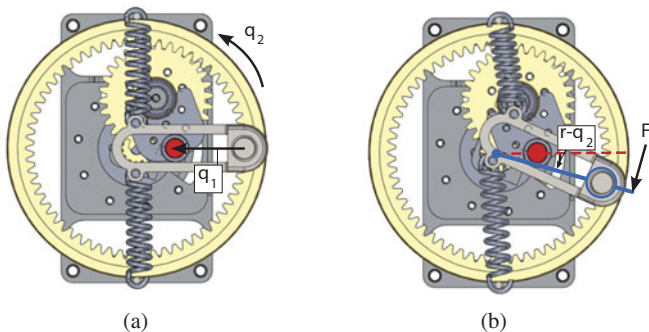
This article has been accepted for inclusion in a future issue of this journal. Content is final as presented, with the exception of pagination.

4   IEEE/ASME TRANSACTIONS ON MECHATRONICS

Fig. 6.   View of the lever arm mechanism connected to the springs. Degree of freedom q_1 is the pivot location, q_2 is the rotation of the actuator frame (consisting of everything shown in the figure) with respect to the fixed reference frame, and $r - q_2$ is the deflection of the output from the equilibrium output position. It can be seen that when a load F is applied to the output, the lever arm rotates around the pivot causing the spring tension to change. (a) Springs only pretensioned. (b) Springs tensioned due to the load on the output.
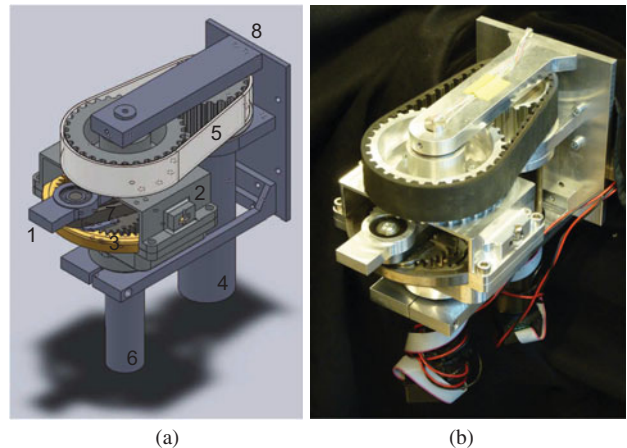

Fig. 7.   CAD view and photo of the vsaUT-II variable stiffness actuator (labels as in Fig. 2). (a) CAD drawing. (b) Physical prototype.

TABLE I
DESIRED SPECIFICATIONS OF THE VSAUT-II

Property	Unit	Value
Peak torque	[Nm]	60
Nominal torque	[Nm]	15
Nominal speed	[rad/s]	π
Active rotation angle	[rad]	π
Passive rotation angle	[rad]	± 0.35
Min. $\leftrightarrow$ max. stiffness variation time	[s]	0.6

rotates around the center of the frame and the other end is connected to two linear extension springs, antagonistically attached and connected to the rotating actuator frame. The ring gear of the planetary gears mechanism is connected to the rotating actuator frame as well, with degree of freedom q_2. Rotating the frame with respect to the fixed reference frame ($\dot{q}_2 \neq 0$) corresponds to the rotation of the equilibrium output position q_2 and the rotation of the straight pivot path q_1. Two different scenarios are depicted in Fig. 6, i.e., (a) shows the pretensioned springs and (b) shows the lever arm, rotated around the pivot point due to an output load F that changes the tension of the springs.

The degree of freedom q_1 determines the output stiffness setting, which, for the vsaUT-II, is given by [16]

$$K := \frac{\partial F}{\partial r} = 2kl^2 \frac{(l - q_1)^2}{q_1^2} \cos(2(r - q_2)) \qquad (6)$$

where k is the elastic constant of the internal elastic elements, i.e., linear mechanical extension springs, l is the lever arm length along which the pivot can be moved with degree of freedom $q_1 \in [0, l]$, the degree of freedom q_2 is the angle of the rotating actuator frame, and r is the output deflection, both with respect to the fixed reference frame.

Due to this particular design of the variable transmission ratio lever arm, the output stiffness can be changed without affecting the elongation of the springs. This not only holds at the actuator equilibrium position $r - q_2 = 0$, but also for a relative output position $r - q_2 \neq 0$ [11].

E. Actuator Design

Fig. 7 shows a CAD drawing and the physical prototype, with labels as in Section II-B. The desired specifications, used during the design process, are reported in Table I. The active rotation angle is the maximum amplitude of the output motion r and the passive rotation angle $r - q_2$ is the maximum angle of the output at minimum output stiffness.

III.   PROTOTYPE MODELING AND REALIZATION

In this Section, we focus on the model of the prototype and its realization. First, we elaborate on the choice of springs for the prototype. Then, from Section III-B, the lumped parameter model of the actuator is presented as various subsystems and, where applicable, the measurements to find the parameters associated to the dominant behavior of the system are presented.

A. Spring Characteristics

The output stiffness of the actuator is given by (6). This equation is dependent on the elastic constant k of the springs that are used in the actuator. However, the total stiffness range does not depend on k, since the design of the actuator ensures, theoretically, an infinite stiffness range by positioning the pivot point along the lever arm. In practice, the stiffness ranges from almost zero to a very high stiffness, limited by parasitic mechanical compliance. The stiffness changing resolution (locally defined as $\frac{\partial K}{\partial q_1}$), however, does change for springs with different elastic constants. Since this prototype is intended as a proof of concept, no requirements are posed on the output stiffness profile or energy storing capacity. Arbitrary springs with an elastic constant $k = 1886$ N/m are used.

B. Motor Model

Two Maxon graphite brushed dc-motors are used for actuating the two internal degrees of freedom q_1 and q_2, as described in Section II. The sun gear is driven by a Maxon 24 V 20 W RE-25 dc-motor, connected to a Maxon GP26B planetary gearbox with speed reduction ratio 84. The torque at the output is provided

This article has been accepted for inclusion in a future issue of this journal. Content is final as presented, with the exception of pagination.

GROOTHUIS *et al.*: VARIABLE STIFFNESS ACTUATOR vsaUT-II: MECHANICAL DESIGN, MODELING, AND IDENTIFICATION 5

TABLE II
MOTOR MODEL PARAMETERS

Parameter	Unit	Maxon RE-20	Maxon RE-40
Inductance	[H]	$2.38 \cdot 10^{-4}$	$8.23 \cdot 10^{-5}$
Resistance	[Ω]	2.19	0.317
Gyration constant	[$\frac{\text{Nm}}{\text{A}}$]	$2.34 \cdot 10^{-2}$	$3.02 \cdot 10^{-2}$
Motor shaft inertia	[kg m^2]	$1.07 \cdot 10^{-6}$	$1.38 \cdot 10^{-5}$
Friction	[$\frac{\text{Ns}}{\text{m}}$]	$6.4 \cdot 10^{-6}$	$3.0 \cdot 10^{-6}$

TABLE III
GEARBOX MODEL PARAMETERS

Parameter	Unit	Maxon GP26B	Maxon GP42C
Speed reduction ratio	–	84	156
Max. cont. output torque	[Nm]	1.3	15
Max. efficiency	–	0.59	0.72
Scaling parameter α	–	7	7
Inertia at input	[kg m^2]	$4 \cdot 10^{-8}$	$9.1 \cdot 10^{-7}$

by a Maxon 24 V 150 W RE-40 dc-motor coupled to a Maxon GP42C planetary gearbox with speed reduction ratio 156 [20]. The motor parameters are taken from the datasheets. However, friction was not specified and since it determines the no-load speed of the motor, it was iteratively tuned to a value where the simulated no-load speed of the motor model equals the specified no-load speed, upon actuation with a constant voltage of 24 V. Table II shows the motor parameters.

C. Gearbox Model

Since high energy efficiency is often a goal in the application of a variable stiffness actuator, an accurate energy description in the model is desired. Therefore, a gearbox model with losses is proposed here, as opposed to a lossless gearbox where only the (power-continuous) transmission ratio is taken into account. The losses are modeled as a decrease in gearbox output torque (load torque) by

$$\tau_{\text{load}} = n \cdot \tau_{\text{in}} - \tau_{\text{loss}}$$

where $n > 1$ is the speed reduction ratio of the gearbox.

The gearbox efficiency is a function of the load torque, where losses are primarily due to friction in the bearings and meshing of the gear teeth. At the maximum continuous torque at the output of the gearbox, the efficiency is at its maximum, while greatly decreasing for small loads. The gearbox efficiency versus torque function is assumed to be an exponential function [20], [21], i.e.,

$$\eta(\tau) = \eta_{\text{max}} \cdot \left(1 - e^{-\alpha \frac{|\tau_o|}{\tau_{\text{max}}}} \right)$$

where $\eta(\tau) \in (0, 1]$ is the efficiency of the gearbox, $\eta_{\text{max}} \in (0, 1]$ is the maximum efficiency, τ_o is the ideal (lossless) output torque, τ_{max} is the specified maximum continuous torque at the gearbox output, and α is a scaling parameter to adjust the steepness of the exponential function. The loss torque τ_{loss} is a fraction of the input torque and is given by

$$\tau_{\text{loss}} = n \cdot \tau_{\text{in}} \cdot (1 - \eta(\tau)).$$

Besides the losses, the rotating gearbox parts have inertia specified as the moment of inertia at the motor shaft. This has also been incorporated in the model. Table III shows the parameters used in the gearbox models.

The simulated behavior of this model can be seen in Fig. 8. The parameters of the Maxon GP26B gearbox are used to show the behavior of the gearbox while driving an inertial load. An ideal torque source applies a linearly increasing torque at the input of the gearbox. It can be seen that for small input torques the efficiency is indeed small. The efficiency increases expo-
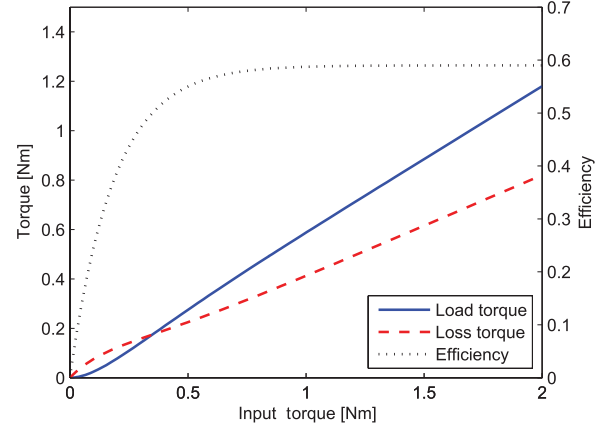

Fig. 8. Simulation of the gearbox model where losses due to the bearings and internal gear meshing are incorporated. The efficiency is low for low input torques and increases exponentially for increasing input torques.

nentially if the torque is increased and reaches its final value of 0.59 at an input torque of 1.3 N·m, i.e., the maximum continuous torque of the gearbox. If the torque is increased further, i.e., if the gearbox is peak loaded, then the efficiency does not increase.

D. Planetary Gears System

As described in Section II-C, a linear motion is achieved by rotation through a planetary gears system. This means that the pivot can track a straight line along the lever arm, as to change the apparent output stiffness. Equations for degree of freedom q_1 and its rate of change $\dot{q}_1$ were derived in (4) and (5). In this specific case, the constant parameters in the equations are: $D_p = 45.5$ mm, $N_r = 60$, $N_p = 30$, $N_c = 31$, and $N_s = 14$.

The inertia of the gears at their center of rotation is approximated by the inertia of a solid disc with radius R and (measured) mass m, i.e., $I = \frac{1}{2} m R^2$. For the planet gear, this means $I_p = 3.0 \times 10^{-5}$ kg · m^2 at $\dot{\theta}_p$ and, for the sun gear, it means $I_s = 2.4 \times 10^{-7}$ kg · m^2 at $\dot{\theta}_s$. The inertia of the displaced planet gear at ω_{pc} is approximated as $I_{\text{pc}} = 9.0 \times 10^{-5}$ kg · m^2.

Note that this analysis describes the dynamics of degree of freedom q_1, identified by the motor, the gearbox, and the planetary gears mechanism.

E. Timing Belt Transmission

As stated in Section II-D, to transmit the power from the motor to the rest of the device, a timing belt transmission is used. This consists of two pulleys, i.e., an input and an output pulley, with a teeth ratio of $32/22 \approx 1.45$, and a Misumi P8M timing belt, pretensioned using an eccentric mechanism with

1.5 mm eccentricity, connecting the two pulleys. The timing belt is modeled as a linear elastic connection between the two tangential velocities of both pulleys.

The actuator design enables the adjustment of the output stiffness K from, theoretically, zero ($q_1 = l$) to infinite ($q_1 = 0$) stiffness. The (finite) maximum stiffness of the actuator was measured and the corresponding compliance is assumed to be concentrated in the elasticity of the timing belt, and thus the internal parts are assumed rigid. The maximum output stiffness $K_{\max}$ is found to be 948 Nm/rad. This can be converted to the linear elasticity in the timing belt by using the output pulley radius $r_{\mathrm{op}} = 41$ mm, i.e., $C_{\mathrm{belt}} = \frac{K_{\max}}{r_{\mathrm{op}}^2} = 564$ kN/m.

F. Actuated Device

The actuated device is defined as the subsystem that is moved by the degree of freedom q_2, i.e., the combination of the planetary gears system, the motor and the gearbox for the actuation of q_1, the rotating actuator frame and the output pulley. Note that the output bar should not be considered here. This part is modeled as a rotating mass subject to friction.

1) Inertia: The initial estimate of the inertia of the actuated device around its central axis I_{ad} is based on a rotating solid disc of radius $R = 45$ mm with a measured mass of $m = 1.2$ kg, i.e., $I_{\mathrm{ad}} = 1.2 \cdot 10^{-3}$ kg $\cdot$ m^2.

The inertia of an electric motor at its output shaft can be reflected to an equivalent inertia at its gearbox shaft by multiplying the motor inertia with the square of the gearbox speed reduction ratio. By doing this, it is shown that the device inertia I_{ad} is much smaller than this transformed inertia, which means that I_{ad} can be neglected, i.e., $I_{\mathrm{RE}-40} \cdot n_{\mathrm{GP42C}}^2 = 0.34$ kg $\cdot$ m$^2 \gg 1.2 \cdot 10^{-3}$ kg $\cdot$ m^2.

2) Friction: The friction while rotating the actuated device is modeled as linear viscous friction and assumed concentrated at the degree of freedom q_2. The friction parameter was found by measuring the damping effect in the prototype after actuating q_2 from an initial angle of -0.4 rad with a constant current in the motor of 0.5 A for $t \in [0, 0.5)$ s. This test has also been performed in simulations: the additional friction at q_2 in the model, besides friction due to the large motor and gearbox and timing belt transmission, has been iteratively adjusted as to match the simulated behavior to the measurement. A friction parameter of 0.55 N s/m has been found, as shown in Fig. 9. Only during the deceleration phase, a deviation can be seen.

Note that this analysis describes the dynamics of degree of freedom q_2, identified by the motor and gearbox, the timing belt transmission and the actuated device.

G. Output Link

The output link is the part where the load can be attached and during tests a solid aluminium bar was fixed to the output. Although the inertia found here is only valid for the particular setup used, the friction measurement is valid in general.

1) Inertia: The initial inertia estimate is based on a solid rod with length $L = 350$ mm and a measured mass $m = 0.262$ kg
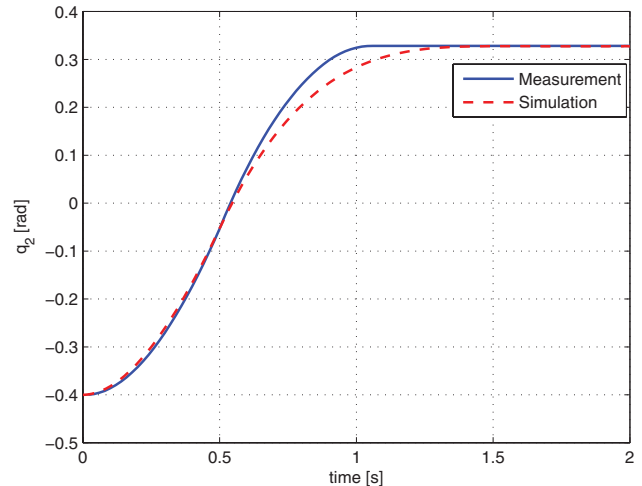

Fig. 9. Behavior of the actuated device after actuating q_2 from an initial angle of 0.4 rad with a constant current in the motor of 0.5 A for $t \in [0, 0.5)$ s. The additional friction at q_2, besides friction due to the motor and gearbox and timing belt transmission, is identified by iteratively matching simulated behavior to the measurements.
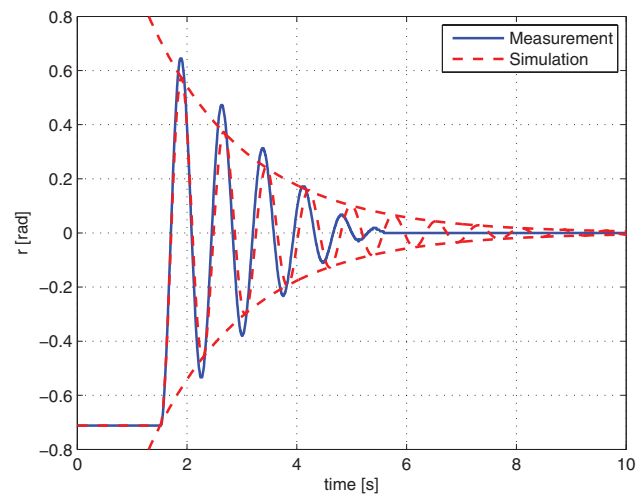

Fig. 10. Output oscillations as measured and simulated. The measured oscillations of the output link were manually triggered, the simulated oscillations, where the exponential amplitude decrease is made explicit, are computed with identified parameters.

rotating about one of its ends, i.e., $I_o = 1.1 \cdot 10^{-2}$ kg $\cdot$ m^2. The actual inertia of the output link was measured by setting the output stiffness to the most compliant setting ($K = 0.7$ Nm/rad, as shown in Section IV), pulling the output to one side, releasing it and measuring the oscillations.

This behavior is shown in Fig. 10 and it is assumed that it can be described by a harmonic oscillator (an underdamped mass-spring system), i.e.,

$$\ddot{r}(t) + \frac{c}{I_o}\dot{r}(t) + \omega_0^2 r(t) = 0 \qquad (7)$$

where the undamped resonance frequency (assumed negligible different from the damped resonance frequency) is given by $\omega_0 = \sqrt{\frac{K}{I_o}}$. Thus, the inertia is found by $I_o = K/\omega_0^2$ or $I_o = K\Delta t^2/4\pi^2$, in which Δt is the time period between two successive peaks of the oscillation. By using the first two

This article has been accepted for inclusion in a future issue of this journal. Content is final as presented, with the exception of pagination.

GROOTHUIS *et al.*: VARIABLE STIFFNESS ACTUATOR vsaUT-II: MECHANICAL DESIGN, MODELING, AND IDENTIFICATION

7

peaks in Fig. 10 ($\Delta t = 0.77$ s), the inertia is found to be $I_o = 1.1 \cdot 10^{-2}$ kg · m^2, which equals the initial estimate.

2) Friction: Two successive peaks in Fig. 10 also define the amount of friction in the subsystem, i.e., the damping coefficient in the model. Again, a linear friction model is assumed: the (small) linear viscous friction in the bearings causes an exponential decay δ in the amplitudes of the oscillation given by $r(t) = \alpha e^{-\delta t}$, where $\delta = \frac{1}{n} \ln \frac{r(t_0)}{r(t_0 + nT)} = 0.56$, in which $r(t_0)$ is the amplitude of the peak at time t_0 and $r(t_0 + nT)$ is the nth peak counting from the peak at $r(t_0)$ (the first and fifth peak were used, i.e., $n = 4$). Since the general solution to (7) is an exponentially decaying harmonic oscillation and is given by

$$r(t) = [A_1 \cos(\omega t) + A_2 \sin(\omega t)] e^{\frac{-c}{2I_o}t}$$

with amplitudes A_1 and A_2 and frequency ω, the friction coefficient c can be found

$$e^{-\delta t} = e^{-\frac{c}{2I_o}t}$$

$$c = 2\delta I_o = 1.2 \cdot 10^{-2} \text{ N s/m.}$$

This damping coefficient is used as the coefficient of friction in the model. The simulated oscillations at the output can be seen in Fig. 10. The measured output behavior is approximated, but decays faster than the corresponding oscillations in the model due to the linear friction model.

H. Sensor System

For controlling the device, sensors are needed to estimate the states of the system. By having an estimate of the degrees of freedom q_1 and q_2 and the output angle r, all other system states and desired properties can be estimated.

An incremental optical encoder Maxon HEDL 5540-500 with 500 counts per revolution (2000 pulses per revolution in quadrature encoding) was mounted on each of the two dc-motors to measure the relative angle of the motors. The angle of the motor θ is converted to the number of pulses p by

$$p = \left\lfloor \theta \cdot \frac{2000}{2\pi} \right\rfloor \tag{8}$$

where $\lfloor \ldots \rfloor$ indicates a floor function of the argument (the number of pulses) to the nearest lower integer number, to model the quantization process. The motor state is represented by the number of pulses from its initial position and therefore by multiplying (8) with $\frac{2\pi}{2000}$, the motor angle is found again, with some lost accuracy due to the quantization. By properly taking the gearbox and the timing belt transmission into account, the degree of freedom q_2 can then be found.

An absolute magnetic encoder (Austria Microsystems AS5043) with a resolution of 10 bits was used to directly measure the output angle r. Similarly to the optical encoders, this sensor was modeled as a quantizer on the angle r with a resolution of $\frac{360°}{1024} \approx 0.35°$/step and added uncertainty due to gain mismatch errors of the AS5043 of $\pm 0.15°$ according to the proposed model in [22].

An absolute calibration of the system can be performed thanks to the absolute magnetic encoder. A homing action on the degree
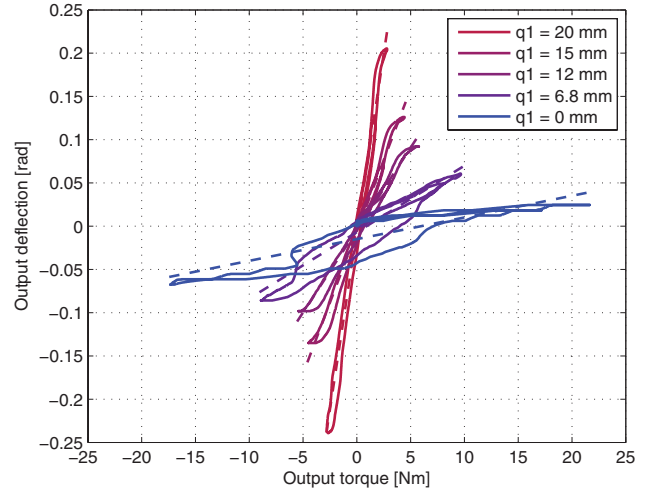

Fig. 11. Output torque versus deflection. For various stiffness settings determined by q_1, a torque is applied on the output and the corresponding deflection is measured. The tangent to these curves at a point gives the compliance of the output at that configuration.

of freedom q_1 to the zero position at an unloaded system calibrates the measurement on q_1 to zero. At this setting, it holds that $q_2 = r$. Therefore, q_2 is in its zero position and can be calibrated as such if r is put in the (absolute) zero position by actuating q_2. All further incremental measurements are performed with respect to this zero position.

IV. SYSTEM MEASUREMENTS

In this Section, we intend to characterize the vsaUT-II prototype by deriving the actuator output torque-deflection diagram. This diagram shows the output deflection $r - q_2$ of the actuation system as a function of the actuator output torque for various output stiffness settings, determined by q_1. The measurement is done with an ATI Mini40 F/T sensor with a maximum force measure capability of 240 N (SI-80-4 metric calibration) and a corresponding resolution of 1/25 N. The sensor is attached to the output link at 267 mm from the center of rotation and an external force is applied to cause an output deflection. A measurement is started in the equilibrium position and is performed as a continuous motion in the positive and negative direction, such that the hysteresis effect caused by energy dissipation (e.g., friction) is shown. The output deflection is measured with the magnetic encoder. The applied torque is calculated by multiplying the measured force and the sensor distance. This measurement is repeated for different pivot positions, i.e., for different output stiffnesses. Note that these measurements are done at the output and, therefore, do not provide transmission efficiency figures, such as the gearbox efficiency as elaborated in Section III.

Fig. 11 shows the result of five of these measurements, namely for pivot positions q_1 at 20, 15, 12, 6.8 and 0 mm. The curves show interpolated data to compensate quantization noise. A dashed line shows the linear least-squares approximation to the curves, of which the slope represents the output compliance. The reciprocal of the linearly approximated slopes represents output stiffness, which is plotted in Fig. 12. In particular, the solid line is the linearly approximated stiffness of the actuator
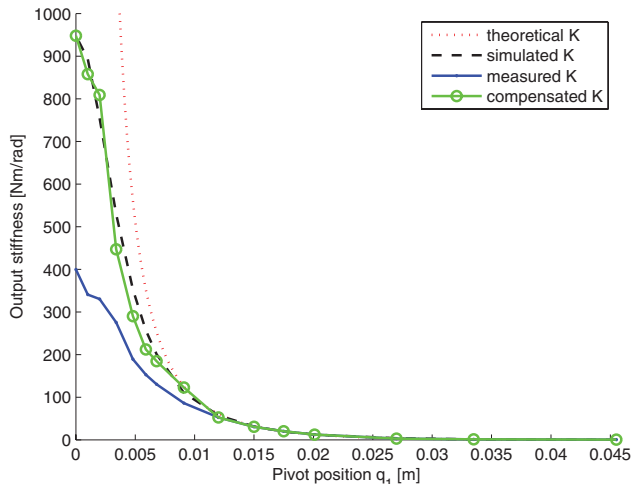
Fig. 12. Output stiffness versus pivot point location – The four graphs (in the legend from top to bottom) represent the theoretical stiffness at $r - q_2 = 0$ rad, the simulated stiffness as found in the model, the measured stiffness from Fig. 11 and the compensated stiffness. It can be seen that the simulated stiffness is approximated well by the compensated stiffness measurement.
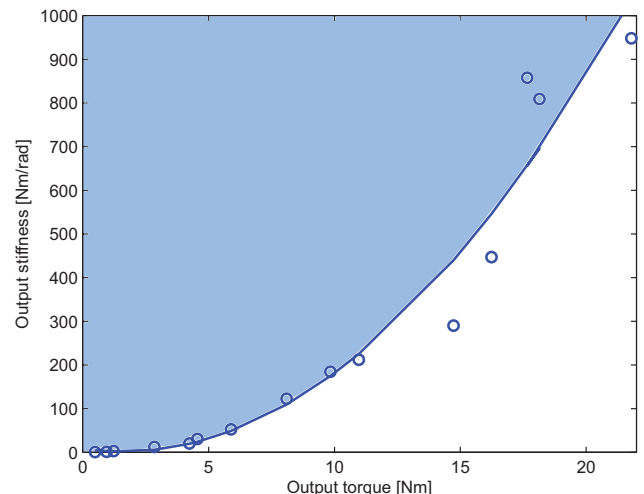

Fig. 13. vsaUT-II workspace-the reachable output stiffness (shaded area) as a function of the output torque.

TABLE IV
OPERATING DATA FOR THE VSAUT-II

	Mechanical		
1	Continuous Output Power	[W]	69.8
2	Nominal Torque	[Nm]	21.8
3	Nominal Speed	[rad/s]	3.2
4	Nom. Stiffness Variation Time: no load	[s]	0.78
5	Nom. Stiffness Variation Time: nom. torque	[s]	0.9
6	Peak (Maximum) Torque	[Nm]	60
7	Maximum Speed	[rad/s]	5.5
8	Maximum Stiffness[1]	[Nm/rad]	948
9	Minimum Stiffness	[Nm/rad]	0.7
10	Maximum Elastic Energy	[J]	0.19
11	Maximum Torque Hysteresis	[%]	12
12	Maximum Deflection: max. stiffness[1]	[°]	2
13	Maximum Deflection: min. stiffness	[°]	40.1
14	Active Rotation Angle	[°]	$\pm$ 28.6
15	Angular Resolution	[°]	0.35
16	Weight	[kg]	2.5
	Electrical		
17	Nominal Voltage	[V]	24
18	Nominal Current	[A]	4
19	Maximum Current	[A]	12
	Control		
20	Voltage Supply	[V]	5 (USB), 7..12
21	Nominal Current	[A]	0.1
22	I/O Protocol	–	RS232

[1] Maximum output stiffness and corresponding maximum deflection are a consequence of the finite structural stiffness of the actuator.

as a function of pivot position q_1. The dotted line represents the theoretical actuator output stiffness (6) for $r - q_2 = 0$, which is zero for $q_1 = l$ and is infinite for $q_1 = 0$.

During the measurement, it has been observed that the setup suffers from a backlash effect due to the connection of input pulley and gearbox. At a certain externally applied output torque, the connection slips briefly before engaging again, as can be seen in the curve for $q_1 = 0$ mm at ± 6 N. This effect has been circumvented by linearly approximating the lower portion of the curve in the third quadrant of Fig. 11. This results in the compensated stiffness curve shown in Fig. 12 (solid curve with open circular marks), which approximates the simulated output stiffness (the dashed curve).

Unlike the theoretical stiffness, which increases to infinity for $q_1 \to 0$, the simulated, measured, and compensated actuator output stiffnesses do not increase to infinity due to the parasitic timing belt compliance. The maximum stiffness is 948 Nm/rad. Since the simulated stiffness closely matches the measured stiffness, it is observed that the model properly represents the stiffness property of the physical system.

The actuator workspace is limited by physical constraints, i.e., the mechanical end-stops of the output and the limit on the maximum spring elongation. Deduced from Fig. 11, an output stiffness versus output torque graph was found, as shown in Fig. 13. The shaded area represents the reachable actuator settings, i.e., the actuator workspace.

The measurement and identification results are summarized in Table IV. It can be shown that the design meets the initial design requirements shown in Table I.

V. DISCUSSION

In this paper, the novel variable stiffness actuator vsaUT-II has been presented. The actuator innovates with the mechanism that is used to move the pivot along a lever arm.

The proposed mechanism uses a rolling transmission, which results in low friction. Furthermore, no linear guides are needed

to constrain the pivot, since its motion is a straight line by design. Finally, a continuous rotation at the input results in a continuous harmonic motion of the pivot, as shown in (4). This means that for reversing the direction of the pivot at the end of its path, there is no need for reversing the input direction, if the lever arm would have length $l = D_r$. This means that the motor inertia does not have to be decellerated when the pivot needs to move in the opposite direction at the end of the lever arm and electrical peak currents are avoided.

However, some drawbacks can also be observed. For instance, the transmission from motor rotation to pivot translation is non-linear, which might increase the control complexity. Moreover, play in the gears was observed during measurements, but this can be compensated.

VI. CONCLUSION

In this paper, we presented the mechanical design, model, and parameters identification of the variable stiffness actuator

This article has been accepted for inclusion in a future issue of this journal. Content is final as presented, with the exception of pagination.

GROOTHUIS *et al.*: VARIABLE STIFFNESS ACTUATOR vsaUT-II: MECHANICAL DESIGN, MODELING, AND IDENTIFICATION 9

vsaUT-II. In this actuation system, the apparent output stiffness and the output position can be varied independently thanks to the realization of a variable transmission between the internal elastic elements' force and the system output force. The variable transmission is implemented by means of a lever arm, whose effective length is given by the relative position of a pivot point along the lever. The innovation of the vsaUT-II is in how the motion of the pivot is realized, namely by means of a modified planetary gears mechanism. A lumped parameter model has been presented and the various system parameters have been identified. System measurements verified the model accuracy and the prototype performance.

REFERENCES

[1] B. Vanderborght, N. Tsagarakis, C. Semini, R. van Ham, and D. Caldwell, "MACCEPA 2.0: Adjustable compliant actuator with stiffening characteristic for energy efficient hopping," in *Proc. IEEE Int. Conf. Robot. Autom.*, 2009, pp. 544–549.

[2] R. Schiavi, G. Grioli, S. Sen, and A. Bicchi, "VSA-II: A novel prototype of variable stiffness actuator for safe and performing robots interacting with humans," in *Proc. IEEE Int. Conf. Robot. Autom.*, 2008, pp. 2171–2176.

[3] S. Wolf and G. Hirzinger, "A new variable stiffness design: Matching requirements of the next robot generation," in *Proc. IEEE Int. Conf. Robot. Autom.*, 2008, pp. 1741–1746.

[4] T. Morita and S. Sugano, "Development of an anthropomorphic force-controlled manipulator WAM-10," in *Proc. IEEE Int. Conf. Adv. Robot.*, 1997, pp. 701–706.

[5] J. Choi, S. Hong, W. Lee, and S. Kang, "A variable stiffness joint using leaf springs for robot manipulators," in *Proc. IEEE Int. Conf. Robot. Autom.*, 2009, pp. 4363–4368.

[6] K. Hollander, T. Sugar, and D. Herring, "Adjustable robotics tendon using a 'Jack Spring'$^{\mathrm{TM}}$," in *Proc. Int. Conf. Rehabil. Robot.*, 2005, pp. 113–118.

[7] B.-S. Kim and J.-B. Song, "Hybrid dual actuator unit: A design of a variable stiffness actuator based on an adjustable moment arm mechanism," in *Proc. IEEE Int. Conf. Robot. Autom.*, 2010, pp. 1655–1660.

[8] A. Jafari, N. Tsagarakis, B. Vanderborght, and D. Caldwell, "A novel actuator with adjustable stiffness (AwAS)," in *Proc. IEEE/RSJ Int. Conf. Intell. Robots Syst.*, 2010, pp. 4201–4206.

[9] A. Jafari, N. Tsagarakis, B. Vanderborght, and D. Caldwell, "AwAS-II: A new actuator with adjustable stiffness based on the novel principle of adaptable pivot point and variable lever ratio," in *Proc. IEEE Int. Conf. Robot. Autom.*, 2011, pp. 4638–4643.

[10] N. G. Tsagarakis, I. Sardellitti, and D. G. Caldwell, "A new variable stiffness actuator (CompAct-VSA): Design and modelling," in *Proc. IEEE/RSJ Int. Conf. Intell. Robots Syst.*, 2011, pp. 378–383.

[11] L. C. Visser, R. Carloni, and S. Stramigioli, "Energy efficient variable stiffness actuators," *IEEE Trans. Robot.*, vol. 27, no. 5, pp. 865–875, Oct. 2011.

[12] M. Fumagalli, E. Barrett, S. Stramigioli, and R. Carloni, "The mVSA-UT: A miniaturized differential mechanism for a continuous rotational variable stiffness actuator," in *Proc. IEEE/EMBS Int. Conf. Biomed. Robot. Biomechatron.*, 2012, pp. 1943–1948.

[13] S. Rao, R. Carloni, and S. Stramigioli, "A novel energy-efficient rotational variable stiffness actuator," in *Proc. IEEE/EMBS Int. Conf. Eng. Med. Biol. Soc.*, 2011, pp. 8175–8178.

[14] L. C. Visser, R. Carloni, and S. Stramigioli, "Variable stiffness actuators: A port-based analysis and a comparison of energy efficiency," in *Proc. IEEE Int. Conf. Robot. Autom.*, 2010, pp. 3279–3284.

[15] R. Carloni, L. C. Visser, and S. Stramigioli, "Variable stiffness actuators: A port-based power-flow analysis," *IEEE Trans. Robot.*, vol. 28, no. 1, pp. 1–11, Feb. 2012.

[16] S. Groothuis, G. Rusticelli, A. Zucchelli, S. Stramigioli, and R. Carloni, "The vsaUT-II: A novel rotational variable stiffness actuator," in *Proc. IEEE Int. Conf. Robot. Autom.*, 2012, pp. 3355–3360.

[17] S. Groothuis. (2011). "Design, modeling and control of a rotational variable stiffness actuator," M.S. thesis, Univ. Twente, [Online]. Available: https://www.ce.utwente.nl/aigaion/publications/show/2003

[18] I. Thorson and D. Caldwell, "A nonlinear series elastic actuator for highly dynamic motions," in *Proc. IEEE/RSJ Int. Conf. Intell. Robots Syst.*, 2011, pp. 390–394.

[19] D. W. Dudley, *Gear Handbook*. New York, NY, USA: McGraw-Hill, 1962.

[20] Maxon Program 2011/2012, (2012). [Online]. Available: Maxon Motor, http://www.maxonmotor.com

[21] C. Pelchen, C. Schweiger, and M. Otter, "Modeling and simulating the efficiency of gearboxes and of planetary gearboxes," in *Proc. Int. Modelica Conf.*, 2002, pp. 257–266.

[22] *AS5043 Datasheet*, Austria Microsystems, Unterpremstaetten, Austria, Apr. 2009.

Stefan S. Groothuis received the M.Sc. degree in mechatronics from the University of Twente, Enschede, The Netherlands, in 2011, where he is currently working toward the Ph.D. degree in the Robotics and Mechatronics Group.

His main research interests include robotic manipulation, novel actuators and modeling, and control of dynamical systems.

Giacomo Rusticelli received the M.Sc. degree in mechanical engineering from the University of Bologna, Bologna, Italy, in 2011.

He is currently with GIMA, Bologna, Italy, where he is performing research and development in the field of packaging machines.

Andrea Zucchelli received the M.Sc. and Ph.D. degrees in nuclear engineering from the University of Bologna, Bologna, Italy.

He is an Assistant Professor at the University of Bologna. His research interests include the study and the development of criteria for the design of machine elements and the development of advanced composite materials, and their usage for the design and construction of lightweight components.

Dr. Zucchelli is an active member of the Research Group on Electrospinning and an associate member of the National Association on Experimental Mechanics (AIAS).

Stefano Stramigioli (SM'03) received the M.Sc. degree from the University of Bologna, Bologna, Italy, and the Ph.D. degree from the Delft University of Technology, Delft, The Netherlands, in 1992 and 1998, respectively, (both *cum laude*).

He is currently a Full Professor of Advanced Robotics and the Chair Holder of the Robotics and Mechatronics Group, University of Twente, Enschede, The Netherlands. He has coauthored more than 150 publications, including four books. He is the Emeritus Editor-in-Chief of the *IEEE Robotics and Automation Magazine* and is currently the Vice President for member activities of the IEEE Robotics and Automation Society.

Raffaella Carloni (M'08) received the M.Sc. and Ph.D. degrees from the University of Bologna, Bologna, Italy.

She is an Assistant Professor in the Robotics and Mechatronics Group, University of Twente, Enschede, The Netherlands. Her research interests include robotic manipulation, control of complex dynamical systems, novel actuators for locomotion, and prosthetic devices.

Dr. Carloni has been an Associate Editor of the *IEEE Robotics and Automation Magazine* since 2012 and a member of the IFAC Technical Committee on Robotics since 2012.